Structure
Review

Structural Analysis of Supramolecular Assemblies by Cryo-Electron Tomography

Jan Harapin,[1] Matthias Eibauer,[1] and Ohad Medalia[1,2,*]
[1]Department of Biochemistry, University of Zurich, Winterthurerstrasse 190, 8057 Zurich, Switzerland
[2]Department of Life Sciences and the National Institute for Biotechnology in the Negev, Ben-Gurion University, Beer-Sheva, 84105 Israel
*Correspondence: omedalia@bioc.uzh.ch
http://dx.doi.org/10.1016/j.str.2013.08.003

Structural analysis of macromolecular assemblies in their physiological environment is a challenging task that is instrumental in answering fundamental questions in cellular and molecular structural biology. The continuous development of computational and analytical tools for cryo-electron tomography (cryo-ET) enables the study of these assemblies at a resolution of a few nanometers. Through the implementation of thinning procedures, cryo-ET can now be applied to the reconstruction of macromolecular structures located inside thick regions of vitrified cells and tissues, thus becoming a central tool for structural determinations in various biological disciplines. Here, we focus on the successful in situ applications of cryo-ET to reveal structures of macromolecular complexes within eukaryotic cells.

Macromolecular assemblies are central players in many cellular processes that influence the dynamic intracellular architecture of cells. For instance, cytoskeletal processes occur within fractions of a second, resulting in major remodeling of the cytoplasm and the overall cellular morphology (Diez et al., 2005). Various experimental tools for analyzing multicomponent macromolecular structures inside cells have been developed in order to advance the current understanding of functional interactions and dynamic properties of different cellular processes. More specifically, advances in imaging and image analysis techniques have enabled the structural analysis of macromolecular assemblies to reach resolutions on the previously unattainable nanometer scale, thus providing novel insights into the local and global organization of functional modules and cellular networks (Fridman et al., 2012; Lučić et al., 2008).

Cryo-electron tomography (cryo-ET) has a pivotal role in cellular biology (Al-Amoudi et al., 2007; Maimon et al., 2012; Patla et al., 2010), microbiology (Dobro et al., 2013; Kürner et al., 2005; Lieber et al., 2009; Swulius et al., 2011) and virology (Bharat et al., 2012; Meyerson et al., 2011). It can depict a particular cellular scene and provide a three-dimensional (3D) structural map of an unperturbed, vitrified sample, i.e., in a close-to-physiological state (Fridman et al., 2012; Lučić et al., 2005; Yahav et al., 2011). Preserving fine and delicate structural details in a close-to-life state are made possible by the use of rapid freezing, which thus circumvents the deleterious effects of chemical fixatives and dehydration on cellular ultrastructures (Adrian et al., 1984; Dubochet et al., 1988).

In this review, we will focus on the principles and implementation of cryo-ET in the field of cellular and molecular structural biology and discuss the recent technical advances in reconstructing 3D structures of macromolecular complexes within intact cells and organelles. The combination of cryo-ET and single-particle analysis approaches will be discussed in detail with special emphasis on their potential for increasing the final resolution of reconstructed images. Finally, we will discuss complementary sample preparation procedures that enable the application of cryo-ET to large cells and tissues. Although we focus on the application of these techniques to eukaryotic systems, cryo-ET has proven itself instrumental for reconstructing molecular structures in prokaryotes, yielding impressive results (Abrusci et al., 2013; Briegel et al., 2012; Schlimpert et al., 2012; Swulius et al., 2011).

Cryo-ET: Basic Principles

The true power of cryo-ET lies in its ability to directly observe macromolecular densities in situ due to phase contrast between the biological material and the surrounding vitrified ice, bypassing the use of fixatives as well as commonly used contrasting agents such as heavy metal salts (Medalia et al., 2002). Thus, the initial step in preparing biological samples for cryo-ET is vitrification, which is typically performed by plunging into liquid-nitrogen-cooled liquid ethane or high-pressure freezing (HPF) to ensure full hydration and ultrastructure preservation.

During the process of tomographic acquisition, vitrified samples of suitable thickness (<1 μm) are rotated around a defined tilt axis in discrete increments inside the transmission electron microscope (TEM), covering a maximal range of 140°, between −70° and +70° (Frank, 1992). A series of two-dimensional projections, i.e., a "tilt-series," is collected under "low electron dose" conditions (typically <100 $e^{-}/Å^{2}$) to prevent radiation damage to the sample (Dierksen et al., 1992, 1993). The tilt-series is subsequently aligned to a common frame using fiducial markers, i.e., colloidal gold of 10-15 nm in diameter (Amat et al., 2008), or using cross-correlation-based strategies (Castaño-Díez et al., 2010; Sorzano et al., 2009). The aligned tilt-series is then used to reconstruct the 3D volume of the specimen, namely, a tomogram (Frank, 1992). Although the most commonly used algorithm for tomographic reconstruction is the weighted back projection (Radermacher, 1988), alternative algorithms, such as algebraic reconstruction technique (ART) (Gordon et al., 1970) and simultaneous iterative reconstruction technique (SIRT) (Gilbert, 1972), are also in use.

The quality of the final tomogram is directly dependent on the angular increments and the number of recorded two-dimensional images (Horowitz et al., 1997). However, the inherent

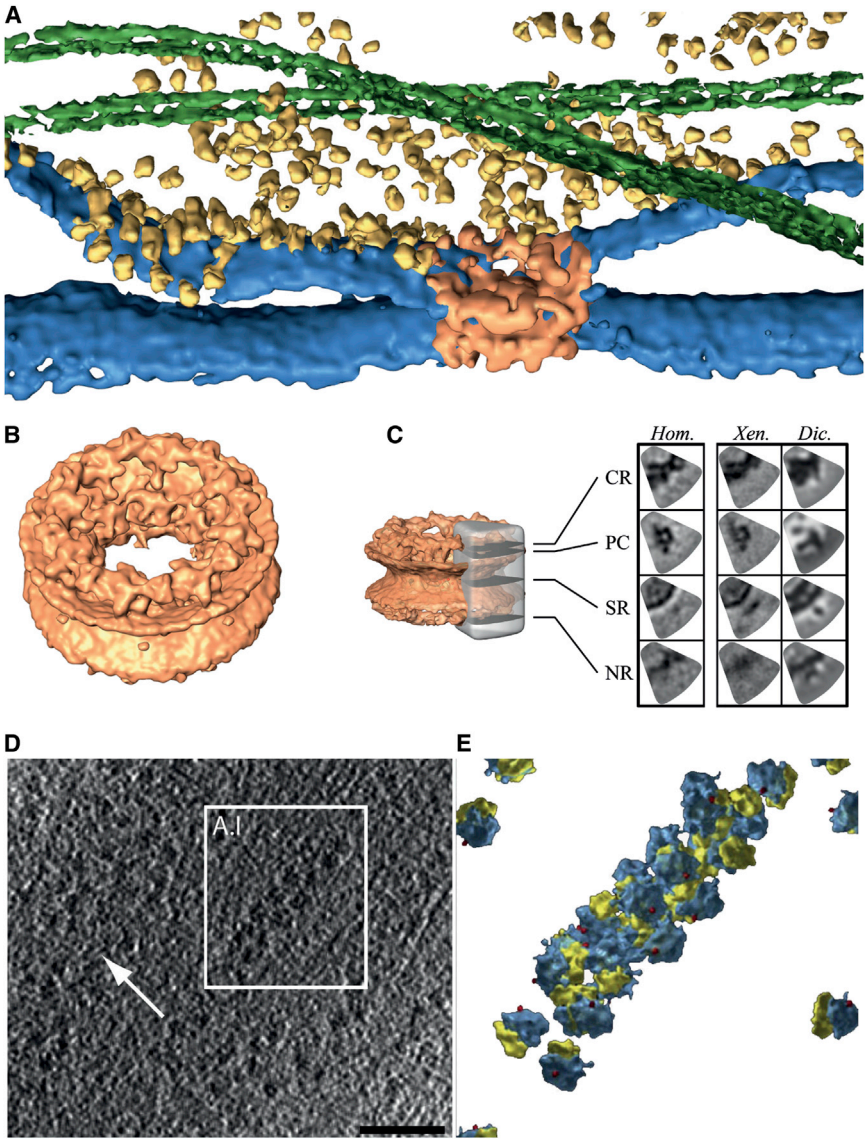

Figure 1. In Situ Subtomogram Averaging
(A) A surface-rendered view of a tomographic reconstruction showing the interior of a U2OS cell. Nuclear membranes (blue), NPCs (orange), microtubules (green) and ribosomes (yellow).
(B) The structure of the *Homo sapiens* NPC as derived by subtomogram averaging.
(C) Comparison of the cytoplasmic ring (CR), the peripheral channel (PC), the spoke ring (SR) and the nuclear ring (NR) in NPC protomer slices of *H. sapiens*, *X. laevis*, and *D. discoideum*.
(D) Tomographic slice showing polysomes from intact human cells (white box labeled with A.I indicates the area used for 3D visualization; white arrow indicates local accumulations of monosomes).
(E) 3D model of the polysome from box A.I. Figures 1A–1C reprinted from Maimon et al. (2012). Figures 1D and 1E reprinted with permission from Brandt et al. (2009).

lack of coverage in the high-tilt range (i.e., above −70° and +70°) produces an area of missing information termed ''missing wedge'' because of its appearance in Fourier space, leading to feature elongation and reduced resolution in the direction of the electron beam (Frank, 1992). The missing information can be reduced by acquiring a second tilt-series orthogonal to the first one, e.g., dual-axis tilting (Mastronarde, 1997), thus reducing the missing wedge to <10%. However, aligning the two perpendicular sets of projections remains a challenging task (Iancu et al., 2005).

Reconstructing the Structures of Macromolecular Complexes In Situ

A major advantage of cellular cryo-ET is that intracellular structures and protein complexes, e.g., the actin cytoskeleton, nuclear lamina, nuclear pore complexes (NPCs), and ribosomes, can be imaged in their native context, i.e., within an intact cell (Figures 1D, 2A, 4B, and 4C), and subsequently analyzed by specialized image processing methods (Frangakis and Förster, 2004).

Cellular tomograms containing macromolecular assemblies in multiple copies can be further processed by subtomogram averaging (Bartesaghi and Subramaniam, 2009; Briggs, 2013). The basic goal of this in silico procedure is to combine subtomograms (subvolumes of tomograms) that contain repeating structures, in order to produce a subtomogram average (final structure) with an enhanced resolution and signal-to-noise ratio (SNR) compared to the initial tomograms. The application of subtomogram averaging relies on the successful identification of a complex, structural homogeneity of a complex in the cellular environment, and occurrence of a complex in many different orientations.

In order to generate a subtomogram average with isotropic resolution, as first described by Förster et al. (2005), the missing wedge in the tomographic data has to be filled by orienting and subsequently averaging a sufficiently large number of different views of the macromolecular complex being investigated (Figure 3). The subtomograms are aligned with respect to a common reference, where the rotational part of the alignment is performed by an exhaustive search over a set of equally distributed Euler angles (Stölken et al., 2011). Thereby, the reference is rotated and convoluted with the experimentally realized missing wedge prior to a cross-correlation comparison with the subvolumes. These steps are performed successively for all desired angles. Subsequently, the maximum cross-correlation value indicates the orientation that maximizes the similarity between a subtomogram and the reference (Frangakis et al., 2002), whereas the translation between the volumes is given by the position of the cross-correlation peak (Frank, 2006). In this way a unique rotation and translation can be assigned to each subtomogram.

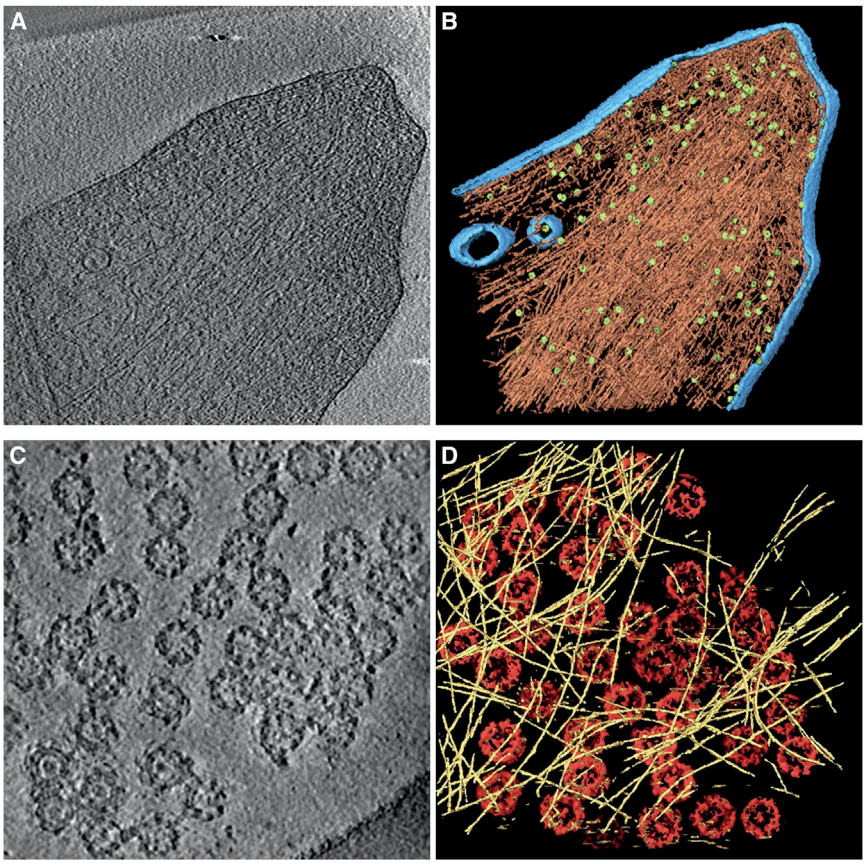

Figure 2. Cryo-ET of Cytoskeletal Elements
(A and B) A 10 nm tomographic slice through a focal adhesion site (A) and a corresponding rendered view of the cellular volume (B). Membranes (blue), actin (red) and adhesion-related particles (green).
(C and D) A 10 nm tomographic slice through a spread nuclear membrane of *X. laevis* ectopically expressing ce-lamins (C) and a corresponding rendered view of the tomographic volume (D). Lamin filaments (yellow), NPCs (red). Figures 2A and 2B reprinted from Patla et al. (2010); Figures 2C and 2D reprinted from Grossman et al. (2012b).

Next, the subtomograms are transformed according to the found parameters, and the aligned stack of volumes is averaged and serves as the reference for the next step. This iterative procedure is performed until the structure no longer changes with subsequent iterations. Finally, the iteratively refined transformations are used to generate the final subtomogram average (Walz et al., 1997). Obviously, the inverse of the calculated rotations describe the original orientations of the macromolecular complexes in the cellular environment. This information can be useful for unveiling the spatial relationship between macromolecules in a physiological assembly such as polysomes (Brandt et al., 2009, 2010) (Figures 1D and 1E). Because of a high value of defocus used in cellular cryo-ET, typically in the range of -6 to -15 μm, the maximal resolution of a subtomogram average is around 3–5 nm. In order to extend the information beyond the first destructive electron interference, a contrast transfer function (CTF) correction can be applied to the projection images, as it is routinely used in single-particle analysis electron microscopy (van Heel et al., 2000). Here, the resulting CTF-corrected tomograms serve as input data for subtomogram averaging.

Two major challenges in applying the CTF correction to tomographic data sets should be resolved. First, the effective value of defocus cannot be accurately determined in an image of thick cells, because of the low electron-dose used to obtain each individual projection. Second, the effective value of defocus varies throughout the entire projection, because of the tilting of the sample (Philippsen et al., 2007). In order to tackle these challenges, an approach called strip-based periodogram averaging was developed by Fernández et al. (2006). The problem of defocus determination can be solved by dividing a projection into subimages with constant values of defocus. These are located parallel to the tilt axis when the tilt-series is eucentric and no major jumps in the beam direction occur. Depending on the tilt angle, the target region for the extraction of the subimages has to be adjusted with a precision threshold. For example, one can use the entire 0° projection image because it has a constant value of defocus over the entire field of view. In contrast, only a small region parallel to the tilt axis of the projections acquired at the highest tilt angles can be used for strip-based periodogram averaging. Once all subimages with constant defocus from a tilt-series have been extracted, they can be averaged. The power spectrum of this periodogram average (Fernandez et al., 1997) has an improved SNR and the Thon rings become more clearly visible. The average defocus value of the tilt-series can now be determined from the periodogram average, using standard methods (Mindell and Grigorieff, 2003). Subsequently, the average defocus value can be used to calculate the defocus value of each pixel in the projections using geometrical parameters of the tilt-series (tilt angle and tilt axis orientation). Finally, the CTF gradient arising from the tilting of the sample can be corrected locally (Winkler et al., 2003).

Other approaches were recently developed that use advanced schemes to determine the effective value of defocus in a tilt-series and to perform proper CTF correction (Eibauer et al., 2012; Xiong et al., 2009; Zanetti et al., 2009). The CTF correction in combination with subtomogram averaging will allow the reconstruction of images of macromolecular complexes in situ, reaching resolutions close to 1 nm in the future.

In recent years additional algorithms were developed in order to tackle the challenge of subtomogram averaging, mainly in order to accelerate the angular part of the search. Examples include approaches that employ spherical harmonics for angular assignments (Bartesaghi et al., 2008; Chen et al., 2013; Xu et al., 2012) and maximum likelihood-based methods (Scheres et al., 2009; Stölken et al., 2011), as well as integrated open-source

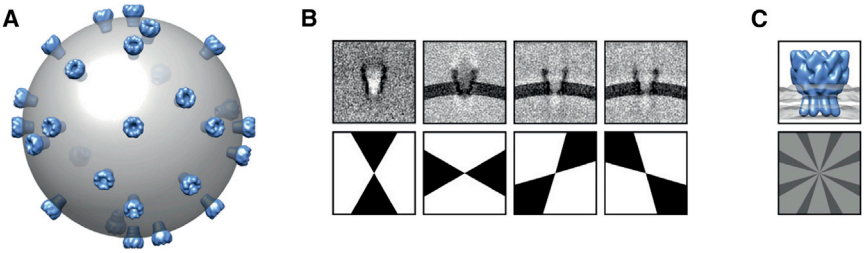

Figure 3. Principles of Subtomogram Averaging

(A–C) A cryo-ET analysis yields a 3D-reconstructed volume (A) (shown schematically). A stack of ***N*** subtomograms of a macromolecular assembly in different orientations is extracted from the cryo-tomograms. These subtomograms have a very low SNR (B, upper panel), and the protein complex is elongated in direction of the electron beam because of the missing wedge, which has the same orientation for all subtomograms. The subtomograms are aligned with respect to a common reference by an exhaustive angular search. The missing wedges of the aligned particles indicate which regions in Fourier space are sampled in the related subtomogram (B, lower panel). Finally, the aligned subtomogram stack is averaged, which improves the SNR by a factor of $\sqrt{N}$ (C, upper panel). Furthermore, the resolution is isotropic, because missing regions in Fourier space are filled (C, lower panel). Figure modified from Eibauer et al. (2012).

software packages for subtomogram averaging that will surely make the procedure more accessible to a wide audience (Castaño-Díez et al., 2012; Hrabe et al., 2012).

The Structure of the NPC as Resolved by Subtomogram Averaging

A successful application of subtomogram averaging, applied to tomograms from intact human cells, is the structural analysis of the NPC (Maimon et al., 2012). NPCs are composed of ~30 different proteins termed nucleoporins (Nups), which are arranged as multimers containing multiple copies (Alber et al., 2007; Cronshaw et al., 2002; Ori et al., 2013; Terry et al., 2007). The architecture of the NPC is largely conserved between lower and higher eukaryotes (Figure 1C), comprising a pseudo-8-fold symmetric central framework termed the spoke complex, a central pore of about 50 nm in diameter, and filamentous structures on the cytoplasmic and nuclear sides of the complex (Elad et al., 2009). On the nuclear face, the NPC is found in close interaction with the nuclear lamina, a meshwork of filamentous protein structures and other associated proteins (Burke and Stewart, 2013).

This humongous macromolecular assembly of over 120 MDa fuses the outer nuclear membrane and the inner nuclear membrane to form aqueous translocation channels. The NPC allows passive diffusion of small molecules and receptor-dependent translocation of large proteins and ribonucleoproteins (Adams and Wente, 2013; Grossman et al., 2012a). Macromolecular cargo usually harbors a specific nuclear localization signal (NLS) or nuclear export signal (NES) that are recognized by transport receptors, mediating cargo passage through the NPC. Receptors referred to as karyopherins chaperone cargo during transport across the NPC by means of hydrophobic interactions with phenylalanine-glycine-rich nucleoporin repeat domains (FG-repeats) (Stewart, 2006; Suntharalingam and Wente, 2003).

Over the last decade, cryo-ET has become a major tool for reconstructing the structure of the NPC by using intact nuclei and nuclear envelopes (NE) with minimal purification steps (Beck et al., 2004; Stoffler et al., 2003). However, variability within the complex and deviations from its 8-fold symmetrical structure limited the resolution to ~8.5 nm. Introducing symmetry-independent averaging procedures allowed computational compensation for the deviations of individual NPC protomers from their putative positions in an 8-fold rotational symmetric structure in both *Dictyostelium discoideum* and *Xenopus laevis* (Beck et al., 2007; Frenkiel-Krispin et al., 2010).

Recently, we have deployed a similar approach to reconstructing the human NPC, using intact cells (Maimon et al., 2012). Tomograms were acquired at thin nuclear regions within cells, ~700 nm, followed by subtomogram averaging analysis that used the symmetry-independent averaging approach (Beck et al., 2007). The result was a detailed structure of the human NPC at a resolution of 6.4 nm. NPCs from three different species were reconstructed using the very same approach at similar resolutions (Figure 1C). All three structures converged to a pseudo-8-fold rotational symmetric architecture with similar values for the outer diameter (~105 nm) and the central channel (~50 nm). However, they exhibited substantial structural differences in the cytoplasmic ring and the peripheral channels, especially between the NPCs of higher and lower eukaryotes (Figure 1C). The structure of the spoke ring shows overall structural similarity between the NPCs of *X. laevis* and *D. discoideum*. Furthermore, the density of the NPCs in the nuclear envelope differs widely across these species rising up to 50 NPCs/μm^2 in *X. laevis* and is significantly less in human cells (Maimon et al., 2012). A more detailed structure that allows for the fine interpretation of the spatial organization and protein composition of the NPCs will surely arise in the future. The combined approach of cryo-ET and 3D averaging over a data set sufficiently large, acquired on a thinner sample, should allow for a final resolution of ~2 nm and make possible the reliable fitting of individual Nup crystal structures into the final tomographic reconstruction.

Cellular Processes

Cryo-ET has been successfully applied to the study of cytoskeleton-based processes (Ben-Harush et al., 2010), allowing for a detailed description of cellular events, such as adhesion (Patla et al., 2010), virus infection (Ibiricu et al., 2013), endocytosis (Swulius et al., 2011), and cytokinesis (Elad et al., 2011). The exact architecture of the actin filaments and the macromolecular assembly of adhesion sites could not be seen using conventional electron microscopy sample preparation methods (Medalia and Geiger, 2010). The architecture of focal adhesions was described in great detail, clearly showing that the actin cytoskeleton is not directly connected to the membrane domain of the adhesion site, namely, the integrin (Figures 2A and 2B). Another example is the elucidation of the intricate organizational properties of the *Caenorhabditis elegans* lamin filaments assembled in *X. laevis* oocytes that show the wild-type filaments to be almost half the previously reported diameter (Grossman et al., 2012b) (Figure 2D).

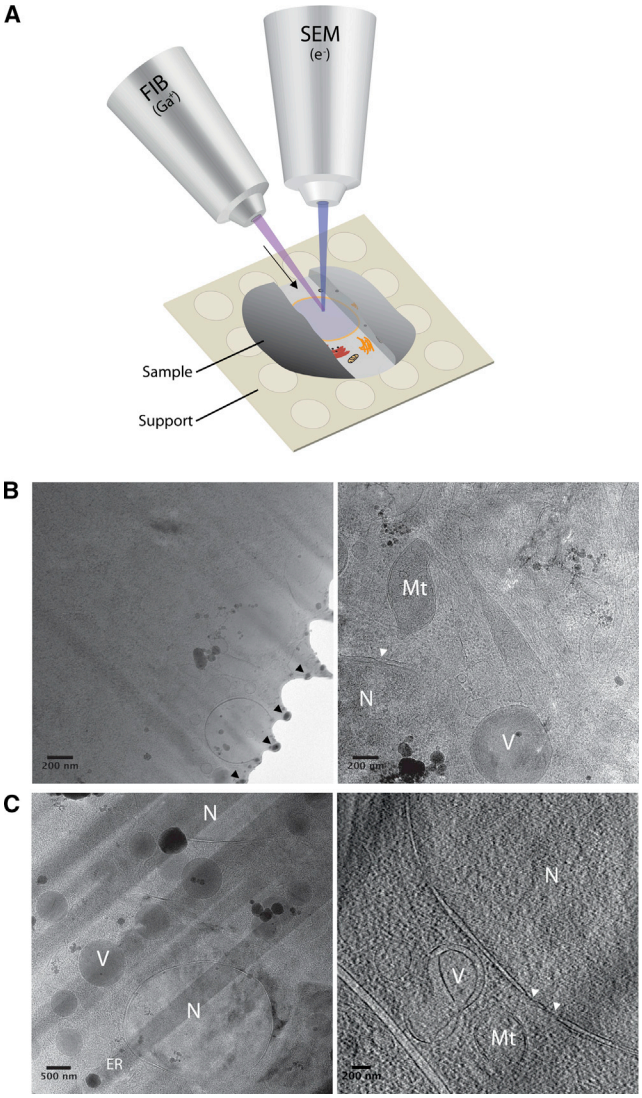

Figure 4. Focused Ion Beam Milling of Vitrified Eukaryotic Samples
(A) Schematic illustration of FIB milling of cells and the production of thin lamellas for subsequent cryo-ET analysis.
(B) Cryo-EM image of a 250 nm thick vitreous lamella produced by FIB milling of a U2Os cell (left) and a higher magnification TEM image indicating crowded cytoplasm.
(C) The application of cryo-FIB to a multicellular specimen is exemplified by imaging the 300 nm thick lamella produced in an early *C. elegans* embryo (left), and a 4 nm slice through a tomographic reconstruction of such a sample. N, nucleus; Mt, mitochondria; V, vesicles; ER, endoplasmatic reticulum; white arrowheads, Ga^+ ion deposits at the edges of the lamella; black arrows indicate, NPCs; black arrow, direction of FIB milling.

Cryo-ET has several fundamental limitations that warrant the use of additional methods in order to produce high-quality tomograms in which molecular complexes can be identified and localized. These issues arise mainly from limited resolution, low SNR, and a limited field of view (only covers 3–4 μm^2 of a cell) and can be overcome, for example, by a correlative light and electron microscopy approach (Lučić et al., 2008) (Fridman et al., 2012). In such a way, one can localize specific molecules with fluorescence-based microscopy and subsequently acquire cryo-tomograms to reveal the cellular ultrastructure at these sites (Jun et al., 2011; Patla et al., 2010; Swulius et al., 2011).

Another example of such limitations is the specimen thickness. Samples exceeding 1 μm in thickness can barely be studied in toto and require preprocessing, such as cryo-sectioning, before tomographic analysis. Several laboratories have devoted substantial efforts to establishing robust thinning procedures (Al-Amoudi et al., 2007; Bokstad et al., 2012; Marko et al., 2006). Cryo-electron microscopy of vitrified sections (CEMOVIS) was successfully applied to reconstructing 3D images of both prokaryotic and eukaryotic cells, as well as some tissues (Al-Amoudi et al., 2003, 2004, 2005, 2007; Hsieh et al., 2002; Pierson et al., 2011). However, the production of thick cryo-sections (300–500 nm) remains a challenging task, and the sections are riddled with sectioning-associated artifacts, such as physical compressions, knife marks, and other distortions. These perturbations are readily observed in the tomographic reconstructions and are keeping this approach from widespread use. In order to be able to apply cryo-ET to thick specimens, such as whole cells and tissues, one must be able to produce a vitrified area of suitable thickness (<500 nm). Thus, the need arose for a robust solution to conventional sample thinning procedures.

Focused Ion Beam Milling for Cryo-ET of Cells and Tissues

Focused ion beam (FIB) technology has already been routinely applied in the field of material sciences in order to manipulate sample thickness and gain insight into so far inaccessible interiors of complex materials (MoberlyChan and Schalek, 2007). In biology, this technique offers a broad range of applications for sequential imaging of plastic embedded samples at room temperature, allowing full-range structural reconstructions (Bennett et al., 2009; Bushby et al., 2011; Heymann et al., 2006). It provides highly resolved views on membranes, up to 5 nm (Kreshuk et al., 2011). However, a 3D structure of macromolecular complexes cannot be reconstructed in great detail because of fixation, dehydration, staining with heavy metal salts, and embedding of the specimen into resins (Bushby et al., 2011).

The application of FIB technology to biological samples under cryogenic conditions is an emerging technology for the production of thin, vitrified specimens for cryo-ET analysis (Marko et al., 2006, 2007; Rigort et al., 2012; Wang et al., 2012). Biological material applied to EM grids can be vitrified by plunge-freezing or high-pressure freezing (HPF) and directly transferred to the cryo-FIB without further processing or use of chemical fixatives and stains. The sample is then thinned by a Ga^+ ion beam at a velocity sufficiently high to overcome the surface binding energies of the sample, consequentially ejecting atoms and leaving a thinned surface (Giannuzzi, 2005). Thus, lamellas of various thicknesses, suitable for cryo-tomography, can be readily produced (Figure 4A). Finally, the EM grid is transferred into the transmission electron microscope for tomographic analysis. High-quality tomograms of biological samples (Rigort et al., 2012), regardless of the original cellular thickness, can be acquired, opening up a plethora of directions for studying the structural and functional organization of both cells and tissues, e.g., human cells and embryos of *C. elegans* (Figures 4B and 4C, respectively). The quality of these tomograms makes possible the application of subtomogram averaging techniques

(Rigort et al., 2012) to the reconstruction of macromolecular complexes in tissues within reach.

Several considerations have to be taken into account throughout the procedure. In order to avoid devitrification and surface contamination of the thinned area, the sample needs to be kept under high-vacuum and cryogenic conditions, as well as be physically shielded with a shutter during the transfer between the different devices used in this kind of a setup. Furthermore, the duration of the milling and the intensity of the ion beam should be kept at a minimum in order to ensure minimal heat transfer to the sample (Marko et al., 2007). The milling of biological samples is performed relatively fast (compared with plastic embedded samples) and at ''grazing'' angles. Thus, the effects of SEM imaging, used primarily for finding regions of interest, and the implantation of Ga+ ions can be considered negligible (Rigort et al., 2010). The straightforward control over the milling process, the possibility of choosing from a wide variety of acceleration voltages and doses of the FIB column, and the design of a milling strategy, depending on the topology of the vitrified biological sample, will ensure the widespread use of this procedure in the near future.

Future Perspectives

Cryo-ET is a pivotal tool for studying cellular architecture and macromolecules in their native environment. In conjunction with subtomogram averaging, it can describe the structural architecture of macromolecular complexes in situ. Extending the application of this method and developing novel image processing algorithms will surely provide an optimal interface for determining cellular structures and following biological processes at high resolution. Sample preparation techniques, such as the cryo-FIB, will eventually make the study of developmental processes from a structural perspective possible. Macromolecular complexes could then be reconstructed at specific stages of development. This will give exciting insight into the macromolecular remodeling within complex organisms.

The achievable resolution in cryo-tomography is hampered by the large sample thickness and the low SNR, resulting in a restricted resolution range (2–4 nm) compared to single-particle analysis reconstructions (Lučić et al., 2005). Thus, hardware developments and improvements in electron microscopy accessories will eventually make increasing the resolution and the SNR of cellular tomograms possible. In particular, introducing direct-electron detectors will allow the acquisition of higher quality data (McMullan et al., 2009). This will have profound effects on the sample integrity because higher quality data will decrease the amount of electrons required to obtain a given resolution, thus ensuring less irradiation of the sample. Data collection routines will be further optimized, leading to the acquisition of larger data sets from which critical parameters, such as defocus, can be reliably determined. Within such a body of data, striking the right balance of dose, focus, and geometry for the problem being addressed will become less demanding. More powerful and increasingly user-friendly software for tomographic reconstruction and subtomogram averaging is continuously being developed, making data analysis a routine task (Castaño-Díez et al., 2012; Chen et al., 2013; Hrabe et al., 2012; Meyerson et al., 2011).

A major challenge, at the current resolution of cellular tomograms, remains the identification of individual constituents within macromolecular complexes. This can be overcome by developing new labeling techniques that would enable the identification of specific molecules by cryo-ET. Several approaches have been described that use genetically encoded tags, such as metallothionein (Mercogliano and DeRosier, 2006; Nishino et al., 2007), ''miniSOG'' (Shu et al., 2011), and APEX (Martell et al., 2012). However, these approaches are not yet suitable for close-to-life cryo-ET of cells and tissues. Thus, there is a fundamental need for the design of a GFP analog for electron microscopy that would provide a general solution for the in situ identification of complexes whose structure is not yet determined or which intimately interact to form large assemblies. The development of novel labeling approaches, the improved resolution of cryo-electron microscopy, and the ability to reconstruct 3D volumes of tissues and cells in a hydrated state are likely to revolutionize cellular and molecular structural biology and our understanding of basic processes in biology.

ACKNOWLEDGMENTS

We thank Dr. Monika Zwerger and Dr. Tanuj K. Sapra for their critical reading of our manuscript. This work was supported by a European Research Council Starting Grant (243047 INCEL) and a Swiss National Science Foundation Grant (SNSF 31003A_141083/1).

REFERENCES

Abrusci, P., Vergara-Irigaray, M., Johnson, S., Beeby, M.D., Hendrixson, D.R., Roversi, P., Friede, M.E., Deane, J.E., Jensen, G.J., Tang, C.M., and Lea, S.M. (2013). Architecture of the major component of the type III secretion system export apparatus. Nat. Struct. Mol. Biol. *20*, 99–104.

Adams, R.L., and Wente, S.R. (2013). Uncovering nuclear pore complexity with innovation. Cell *152*, 1218–1221.

Adrian, M., Dubochet, J., Lepault, J., and McDowall, A.W. (1984). Cryo-electron microscopy of viruses. Nature *308*, 32–36.

Al-Amoudi, A., Dubochet, J., Gnaegi, H., Lüthi, W., and Studer, D. (2003). An oscillating cryo-knife reduces cutting-induced deformation of vitreous ultrathin sections. J. Microsc. *212*, 26–33.

Al-Amoudi, A., Chang, J.J., Leforestier, A., McDowall, A., Salamin, L.M., Norlén, L.P., Richter, K., Blanc, N.S., Studer, D., and Dubochet, J. (2004). Cryo-electron microscopy of vitreous sections. EMBO J. *23*, 3583–3588.

Al-Amoudi, A., Studer, D., and Dubochet, J. (2005). Cutting artefacts and cutting process in vitreous sections for cryo-electron microscopy. J. Struct. Biol. *150*, 109–121.

Al-Amoudi, A., Díez, D.C., Betts, M.J., and Frangakis, A.S. (2007). The molecular architecture of cadherins in native epidermal desmosomes. Nature *450*, 832–837.

Alber, F., Dokudovskaya, S., Veenhoff, L.M., Zhang, W., Kipper, J., Devos, D., Suprapto, A., Karni-Schmidt, O., Williams, R., Chait, B.T., et al. (2007). The molecular architecture of the nuclear pore complex. Nature *450*, 695–701.

Amat, F., Moussavi, F., Comolli, L.R., Elidan, G., Downing, K.H., and Horowitz, M. (2008). Markov random field based automatic image alignment for electron tomography. J. Struct. Biol. *161*, 260–275.

Bartesaghi, A., and Subramaniam, S. (2009). Membrane protein structure determination using cryo-electron tomography and 3D image averaging. Curr. Opin. Struct. Biol. *19*, 402–407.

Bartesaghi, A., Sprechmann, P., Liu, J., Randall, G., Sapiro, G., and Subramaniam, S. (2008). Classification and 3D averaging with missing wedge correction in biological electron tomography. J. Struct. Biol. *162*, 436–450.

Beck, M., Förster, F., Ecke, M., Plitzko, J.M., Melchior, F., Gerisch, G., Baumeister, W., and Medalia, O. (2004). Nuclear pore complex structure and dynamics revealed by cryoelectron tomography. Science *306*, 1387–1390.

Beck, M., Lucić, V., Förster, F., Baumeister, W., and Medalia, O. (2007). Snapshots of nuclear pore complexes in action captured by cryo-electron tomography. Nature *449*, 611–615.

Ben-Harush, K., Maimon, T., Patla, I., Villa, E., and Medalia, O. (2010). Visualizing cellular processes at the molecular level by cryo-electron tomography. J. Cell Sci. *123*, 7–12.

Bennett, A.E., Narayan, K., Shi, D., Hartnell, L.M., Gousset, K., He, H., Lowekamp, B.C., Yoo, T.S., Bliss, D., Freed, E.O., and Subramaniam, S. (2009). Ion-abrasion scanning electron microscopy reveals surface-connected tubular conduits in HIV-infected macrophages. PLoS Pathog. *5*, e1000591.

Bharat, T.A., Davey, N.E., Ulbrich, P., Riches, J.D., de Marco, A., Rumlova, M., Sachse, C., Ruml, T., and Briggs, J.A. (2012). Structure of the immature retroviral capsid at 8 Å resolution by cryo-electron microscopy. Nature *487*, 385–389.

Bokstad, M., Sabanay, H., Dahan, I., Geiger, B., and Medalia, O. (2012). Reconstructing adhesion structures in tissues by cryo-electron tomography of vitrified frozen sections. J. Struct. Biol. *178*, 76–83.

Brandt, F., Etchells, S.A., Ortiz, J.O., Elcock, A.H., Hartl, F.U., and Baumeister, W. (2009). The native 3D organization of bacterial polysomes. Cell *136*, 261–271.

Brandt, F., Carlson, L.A., Hartl, F.U., Baumeister, W., and Grünewald, K. (2010). The three-dimensional organization of polyribosomes in intact human cells. Mol. Cell *39*, 560–569.

Briegel, A., Li, X., Bilwes, A.M., Hughes, K.T., Jensen, G.J., and Crane, B.R. (2012). Bacterial chemoreceptor arrays are hexagonally packed trimers of receptor dimers networked by rings of kinase and coupling proteins. Proc. Natl. Acad. Sci. USA *109*, 3766–3771.

Briggs, J.A. (2013). Structural biology in situ—the potential of subtomogram averaging. Curr. Opin. Struct. Biol. *23*, 261–267.

Burke, B., and Stewart, C.L. (2013). The nuclear lamins: flexibility in function. Nat. Rev. Mol. Cell Biol. *14*, 13–24.

Bushby, A.J., P'ng, K.M., Young, R.D., Pinali, C., Knupp, C., and Quantock, A.J. (2011). Imaging three-dimensional tissue architectures by focused ion beam scanning electron microscopy. Nat. Protoc. *6*, 845–858.

Castaño-Díez, D., Scheffer, M., Al-Amoudi, A., and Frangakis, A.S. (2010). Alignator: a GPU powered software package for robust fiducial-less alignment of cryo tilt-series. J. Struct. Biol. *170*, 117–126.

Castaño-Díez, D., Kudryashev, M., Arheit, M., and Stahlberg, H. (2012). Dynamo: a flexible, user-friendly development tool for subtomogram averaging of cryo-EM data in high-performance computing environments. J. Struct. Biol. *178*, 139–151.

Chen, Y., Pfeffer, S., Hrabe, T., Schuller, J.M., and Förster, F. (2013). Fast and accurate reference-free alignment of subtomograms. J. Struct. Biol. *182*, 235–245.

Cronshaw, J.M., Krutchinsky, A.N., Zhang, W., Chait, B.T., and Matunis, M.J. (2002). Proteomic analysis of the mammalian nuclear pore complex. J. Cell Biol. *158*, 915–927.

Dierksen, K., Typke, D., Hegerl, R., Koster, A.J., and Baumeister, W. (1992). Towards automatic electron tomography. Ultramicroscopy *40*, 71–87.

Dierksen, K., Typke, D., Hegerl, R., and Baumeister, W. (1993). Towards automatic electron tomography II. Implementation of autofocus and low-dose procedures. Ultramicroscopy *49*, 109–120.

Diez, S., Gerisch, G., Anderson, K., Müller-Taubenberger, A., and Bretschneider, T. (2005). Subsecond reorganization of the actin network in cell motility and chemotaxis. Proc. Natl. Acad. Sci. USA *102*, 7601–7606.

Dobro, M.J., Samson, R.Y., Yu, Z., McCullough, J., Ding, H.J., Chong, P.L., Bell, S.D., and Jensen, G.J. (2013). Electron cryotomography of ESCRT assemblies and dividing Sulfolobus cells suggests that spiraling filaments are involved in membrane scission. Mol. Biol. Cell *24*, 2319–2327.

Dubochet, J., Adrian, M., Chang, J.J., Homo, J.C., Lepault, J., McDowall, A.W., and Schultz, P. (1988). Cryo-electron microscopy of vitrified specimens. Q. Rev. Biophys. *21*, 129–228.

Eibauer, M., Hoffmann, C., Plitzko, J.M., Baumeister, W., Nickell, S., and Engelhardt, H. (2012). Unraveling the structure of membrane proteins in situ by transfer function corrected cryo-electron tomography. J. Struct. Biol. *180*, 488–496.

Elad, N., Maimon, T., Frenkiel-Krispin, D., Lim, R.Y., and Medalia, O. (2009). Structural analysis of the nuclear pore complex by integrated approaches. Curr. Opin. Struct. Biol. *19*, 226–232.

Elad, N., Abramovitch, S., Sabanay, H., and Medalia, O. (2011). Microtubule organization in the final stages of cytokinesis as revealed by cryo-electron tomography. J. Cell Sci. *124*, 207–215.

Fernandez, J.J., Sanjurjo, J.R., and Carazo, J.M. (1997). A spectral estimation approach to contrast transfer function detection in electron microscopy. Ultramicroscopy *68*, 267–295.

Fernández, J.J., Li, S., and Crowther, R.A. (2006). CTF determination and correction in electron cryotomography. Ultramicroscopy *106*, 587–596.

Förster, F., Medalia, O., Zauberman, N., Baumeister, W., and Fass, D. (2005). Retrovirus envelope protein complex structure in situ studied by cryo-electron tomography. Proc. Natl. Acad. Sci. USA *102*, 4729–4734.

Frangakis, A.S., Böhm, J., Förster, F., Nickell, S., Nicastro, D., Typke, D., Hegerl, R., and Baumeister, W. (2002). Identification of macromolecular complexes in cryoelectron tomograms of phantom cells. Proc. Natl. Acad. Sci. USA *99*, 14153–14158.

Frangakis, A.S., and Förster, F. (2004). Computational exploration of structural information from cryo-electron tomograms. Curr. Opin. Struct. Biol. *14*, 325–331.

Frank, J. (1992). Electron Tomography: Three-Dimensional Imaging with the Transmission Electron Microscope (New York: Plenum Press).

Frank, J. (2006). Three-Dimensional Electron Microscopy of Macromolecular Assemblies: Visualization of Biological Molecules in Their Native State, Second Edition (Oxford: Oxford University Press).

Frenkiel-Krispin, D., Maco, B., Aebi, U., and Medalia, O. (2010). Structural analysis of a metazoan nuclear pore complex reveals a fused concentric ring architecture. J. Mol. Biol. *395*, 578–586.

Fridman, K., Mader, A., Zwerger, M., Elia, N., and Medalia, O. (2012). Advances in tomography: probing the molecular architecture of cells. Nat. Rev. Mol. Cell Biol. *13*, 736–742.

Giannuzzi, L.A. (2005). Introduction to Focused Ion Beams: Instrumentation, Theory, Techniques and Practice, Softcover Edition (New York: Springer).

Gilbert, P. (1972). Iterative methods for the three-dimensional reconstruction of an object from projections. J. Theor. Biol. *36*, 105–117.

Gordon, R.B., Bender, R., and Herman, G.T. (1970). Algebraic reconstruction techniques (ART) for three-dimensional electron microscopy and x-ray photography. J. Theor. Biol. *29*, 471–481.

Grossman, E., Medalia, O., and Zwerger, M. (2012a). Functional architecture of the nuclear pore complex. Annu. Rev. Biophys. *41*, 557–584.

Grossman, E., Dahan, I., Stick, R., Goldberg, M.W., Gruenbaum, Y., and Medalia, O. (2012b). Filaments assembly of ectopically expressed Caenorhabditis elegans lamin within Xenopus oocytes. J. Struct. Biol. *177*, 113–118.

Heymann, J.A., Hayles, M., Gestmann, I., Giannuzzi, L.A., Lich, B., and Subramaniam, S. (2006). Site-specific 3D imaging of cells and tissues with a dual beam microscope. J. Struct. Biol. *155*, 63–73.

Horowitz, R.A., Koster, A.J., Walz, J., and Woodcock, C.L. (1997). Automated electron microscope tomography of frozen-hydrated chromatin: the irregular three-dimensional zigzag architecture persists in compact, isolated fibers. J. Struct. Biol. *120*, 353–362.

Hrabe, T., Chen, Y., Pfeffer, S., Cuellar, L.K., Mangold, A.V., and Förster, F. (2012). PyTom: a python-based toolbox for localization of macromolecules in cryo-electron tomograms and subtomogram analysis. J. Struct. Biol. *178*, 177–188.

Hsieh, C.E., Marko, M., Frank, J., and Mannella, C.A. (2002). Electron tomographic analysis of frozen-hydrated tissue sections. J. Struct. Biol. *138*, 63–73.

Iancu, C.V., Wright, E.R., Benjamin, J., Tivol, W.F., Dias, D.P., Murphy, G.E., Morrison, R.C., Heymann, J.B., and Jensen, G.J. (2005). A "flip-flop" rotation stage for routine dual-axis electron cryotomography. J. Struct. Biol. *151*, 288–297.

Ibiricu, I., Maurer, U.E., and Grünewald, K. (2013). Characterization of herpes simplex virus type 1 L-particle assembly and egress in hippocampal neurones by electron cryo-tomography. Cell. Microbiol. *15*, 285–291.

Jun, S., Ke, D., Debiec, K., Zhao, G., Meng, X., Ambrose, Z., Gibson, G.A., Watkins, S.C., and Zhang, P. (2011). Direct visualization of HIV-1 with correlative live-cell microscopy and cryo-electron tomography. Structure *19*, 1573–1581.

Kreshuk, A., Straehle, C.N., Sommer, C., Koethe, U., Cantoni, M., Knott, G., and Hamprecht, F.A. (2011). Automated detection and segmentation of synaptic contacts in nearly isotropic serial electron microscopy images. PLoS ONE *6*, e24899.

Kürner, J., Frangakis, A.S., and Baumeister, W. (2005). Cryo-electron tomography reveals the cytoskeletal structure of Spiroplasma melliferum. Science *307*, 436–438.

Lieber, A., Leis, A., Kushmaro, A., Minsky, A., and Medalia, O. (2009). Chromatin organization and radio resistance in the bacterium Gemmata obscuriglobus. J. Bacteriol. *191*, 1439–1445.

Lučić, V., Förster, F., and Baumeister, W. (2005). Structural studies by electron tomography: from cells to molecules. Annu. Rev. Biochem. *74*, 833–865.

Lučić, V., Leis, A., and Baumeister, W. (2008). Cryo-electron tomography of cells: connecting structure and function. Histochem. Cell Biol. *130*, 185–196.

Maimon, T., Elad, N., Dahan, I., and Medalia, O. (2012). The human nuclear pore complex as revealed by cryo-electron tomography. Structure *20*, 998–1006.

Marko, M., Hsieh, C., Moberlychan, W., Mannella, C.A., and Frank, J. (2006). Focused ion beam milling of vitreous water: prospects for an alternative to cryo-ultramicrotomy of frozen-hydrated biological samples. J. Microsc. *222*, 42–47.

Marko, M., Hsieh, C., Schalek, R., Frank, J., and Mannella, C. (2007). Focused-ion-beam thinning of frozen-hydrated biological specimens for cryo-electron microscopy. Nat. Methods *4*, 215–217.

Martell, J.D., Deerinck, T.J., Sancak, Y., Poulos, T.L., Mootha, V.K., Sosinsky, G.E., Ellisman, M.H., and Ting, A.Y. (2012). Engineered ascorbate peroxidase as a genetically encoded reporter for electron microscopy. Nat. Biotechnol. *30*, 1143–1148.

Mastronarde, D.N. (1997). Dual-axis tomography: an approach with alignment methods that preserve resolution. J. Struct. Biol. *120*, 343–352.

McMullan, G., Chen, S., Henderson, R., and Faruqi, A.R. (2009). Detective quantum efficiency of electron area detectors in electron microscopy. Ultramicroscopy *109*, 1126–1143.

Medalia, O., and Geiger, B. (2010). Frontiers of microscopy-based research into cell-matrix adhesions. Curr. Opin. Cell Biol. *22*, 659–668.

Medalia, O., Weber, I., Frangakis, A.S., Nicastro, D., Gerisch, G., and Baumeister, W. (2002). Macromolecular architecture in eukaryotic cells visualized by cryoelectron tomography. Science *298*, 1209–1213.

Mercogliano, C.P., and DeRosier, D.J. (2006). Gold nanocluster formation using metallothionein: mass spectrometry and electron microscopy. J. Mol. Biol. *355*, 211–223.

Meyerson, J.R., White, T.A., Bliss, D., Moran, A., Bartesaghi, A., Borgnia, M.J., de la Cruz, M.J., Schauder, D., Hartnell, L.M., Nandwani, R., et al. (2011). Determination of molecular structures of HIV envelope glycoproteins using cryo-electron tomography and automated sub-tomogram averaging. J. Vis. Exp. Published online December 1, 2011. http://dx.doi.org/10.3791/2770.

Mindell, J.A., and Grigorieff, N. (2003). Accurate determination of local defocus and specimen tilt in electron microscopy. J. Struct. Biol. *142*, 334–347.

MoberlyChan W.J., and Schalek, R. (2007). Ion beam induced surface modulations from nano to pico: optimizing deposition during erosion and erosion during deposition. MRS Proceedings *1059*/2007.

Nishino, Y., Yasunaga, T., and Miyazawa, A. (2007). A genetically encoded metallothionein tag enabling efficient protein detection by electron microscopy. J. Electron Microsc. (Tokyo) *56*, 93–101.

Ori, A., Banterle, N., Iskar, M., Andrés-Pons, A., Escher, C., Khanh Bui, H., Sparks, L., Solis-Mezarino, V., Rinner, O., Bork, P., et al. (2013). Cell type-specific nuclear pores: a case in point for context-dependent stoichiometry of molecular machines. Mol. Syst. Biol. *9*, 648.

Patla, I., Volberg, T., Elad, N., Hirschfeld-Warneken, V., Grashoff, C., Fässler, R., Spatz, J.P., Geiger, B., and Medalia, O. (2010). Dissecting the molecular architecture of integrin adhesion sites by cryo-electron tomography. Nat. Cell Biol. *12*, 909–915.

Philippsen, A., Engel, H.A., and Engel, A. (2007). The contrast-imaging function for tilted specimens. Ultramicroscopy *107*, 202–212.

Pierson, J., Ziese, U., Sani, M., and Peters, P.J. (2011). Exploring vitreous cryosection-induced compression at the macromolecular level using electron cryo-tomography; 80S yeast ribosomes appear unaffected. J. Struct. Biol. *173*, 345–349.

Radermacher, M. (1988). Three-dimensional reconstruction of single particles from random and nonrandom tilt series. J. Electron Microsc. Tech. *9*, 359–394.

Rigort, A., Bäuerlein, F.J., Leis, A., Gruska, M., Hoffmann, C., Laugks, T., Böhm, U., Eibauer, M., Gnaegi, H., Baumeister, W., and Plitzko, J.M. (2010). Micromachining tools and correlative approaches for cellular cryo-electron tomography. J. Struct. Biol. *172*, 169–179.

Rigort, A., Bäuerlein, F.J., Villa, E., Eibauer, M., Laugks, T., Baumeister, W., and Plitzko, J.M. (2012). Focused ion beam micromachining of eukaryotic cells for cryoelectron tomography. Proc. Natl. Acad. Sci. USA *109*, 4449–4454.

Scheres, S.H., Melero, R., Valle, M., and Carazo, J.M. (2009). Averaging of electron subtomograms and random conical tilt reconstructions through likelihood optimization. Structure *17*, 1563–1572.

Schlimpert, S., Klein, E.A., Briegel, A., Hughes, V., Kahnt, J., Bolte, K., Maier, U.G., Brun, Y.V., Jensen, G.J., Gitai, Z., and Thanbichler, M. (2012). General protein diffusion barriers create compartments within bacterial cells. Cell *151*, 1270–1282.

Shu, X., Lev-Ram, V., Deerinck, T.J., Qi, Y., Ramko, E.B., Davidson, M.W., Jin, Y., Ellisman, M.H., and Tsien, R.Y. (2011). A genetically encoded tag for correlated light and electron microscopy of intact cells, tissues, and organisms. PLoS Biol. *9*, e1001041.

Sorzano, C.O., Messaoudi, C., Eibauer, M., Bilbao-Castro, J.R., Hegerl, R., Nickell, S., Marco, S., and Carazo, J.M. (2009). Marker-free image registration of electron tomography tilt-series. BMC Bioinformatics *10*, 124.

Stewart, M. (2006). Structural basis for the nuclear protein import cycle. Biochem. Soc. Trans. *34*, 701–704.

Stoffler, D., Feja, B., Fahrenkrog, B., Walz, J., Typke, D., and Aebi, U. (2003). Cryo-electron tomography provides novel insights into nuclear pore architecture: implications for nucleocytoplasmic transport. J. Mol. Biol. *328*, 119–130.

Stölken, M., Beck, F., Haller, T., Hegerl, R., Gutsche, I., Carazo, J.M., Baumeister, W., Scheres, S.H., and Nickell, S. (2011). Maximum likelihood based classification of electron tomographic data. J. Struct. Biol. *173*, 77–85.

Suntharalingam, M., and Wente, S.R. (2003). Peering through the pore: nuclear pore complex structure, assembly, and function. Dev. Cell *4*, 775–789.

Swulius, M.T., Chen, S., Jane Ding, H., Li, Z., Briegel, A., Pilhofer, M., Tocheva, E.I., Lybarger, S.R., Johnson, T.L., Sandkvist, M., and Jensen, G.J. (2011). Long helical filaments are not seen encircling cells in electron cryotomograms of rod-shaped bacteria. Biochem. Biophys. Res. Commun. *407*, 650–655.

Terry, L.J., Shows, E.B., and Wente, S.R. (2007). Crossing the nuclear envelope: hierarchical regulation of nucleocytoplasmic transport. Science *318*, 1412–1416.

van Heel, M., Gowen, B., Matadeen, R., Orlova, E.V., Finn, R., Pape, T., Cohen, D., Stark, H., Schmidt, R., Schatz, M., and Patwardhan, A. (2000).

Single-particle electron cryo-microscopy: towards atomic resolution. Q. Rev. Biophys. *33*, 307–369.

Walz, J., Typke, D., Nitsch, M., Koster, A.J., Hegerl, R., and Baumeister, W. (1997). Electron tomography of single ice-embedded macromolecules: three-dimensional alignment and classification. J. Struct. Biol. *120*, 387–395.

Wang, K., Strunk, K., Zhao, G., Gray, J.L., and Zhang, P. (2012). 3D structure determination of native mammalian cells using cryo-FIB and cryo-electron tomography. J. Struct. Biol. *180*, 318–326.

Winkler, H.H., Daugherty, R.M., and Audia, J.P. (2003). Cysteine-scanning mutagenesis and thiol modification of the Rickettsia prowazekii ATP/ADP translocase: evidence that TM VIII faces an aqueous channel. Biochemistry *42*, 12562–12569.

Xiong, Q., Morphew, M.K., Schwartz, C.L., Hoenger, A.H., and Mastronarde, D.N. (2009). CTF determination and correction for low dose tomographic tilt series. J. Struct. Biol. *168*, 378–387.

Xu, M., Beck, M., and Alber, F. (2012). High-throughput subtomogram alignment and classification by Fourier space constrained fast volumetric matching. J. Struct. Biol. *178*, 152–164.

Yahav, T., Maimon, T., Grossman, E., Dahan, I., and Medalia, O. (2011). Cryo-electron tomography: gaining insight into cellular processes by structural approaches. Curr. Opin. Struct. Biol. *21*, 670–677.

Zanetti, G., Riches, J.D., Fuller, S.D., and Briggs, J.A. (2009). Contrast transfer function correction applied to cryo-electron tomography and sub-tomogram averaging. J. Struct. Biol. *168*, 305–312.

